This manuscript was prepared for Atmos. Chem. Phys. (Discuss.)
with version 7.7 of the egu LaTeX class egu.cls.
Date: September 27, 2006

ACP-LOGO

3D polarised simulations of space-borne passive mm/sub-mm midlatitude cirrus observations: A case study

C. P. Davis[1], H. C. Pumphrey[1], K. F. Evans[2], S. Buehler[3], and D. L. Wu[4]

[1]Institute of Atmospheric and Environmental Science, University of Edinburgh
[2]Dept. of Atmosphere and oceanic Sciences, University of Colorado
[3]Department of Space Science (IRV), Kiruna, Sweden
[4]NASA Jet Propulsion Laboratory

Abstract. Global observations of ice clouds are needed to improve our understanding of their impact on earth's radiation balance and the water-cycle. Passive mm/sub-mm has some advantages compared to other space-borne cloud-ice remote sensing techniques. This paper presents detailed simulated observations for three such instruments, AMSU-B, CIWSIR, and EOS-MLS. The Monte-Carlo radiative transfer code, ARTS-MC, makes proper account of polarisation and uses 3D spherical geometry. The actual field of view characteristics for each instrument are also accounted for. A 3D midlatitude cirrus scenario is used, which is derived from Chilbolton cloud radar data and a stochastic method for generating 3D ice water content fields. Although the main purpose of the work was to demonstrate the capability of accurately simulating observations of this type, the results suggest that cloud inhomogeneity will affect CIWSIR, and EOSMLS low tangent height observations via the beamfilling effect. Also, the results confirm that preferentially oriented ice crystals will produce significant polarisation effects.

1 Introduction

Probably the greatest uncertainty in future projections of climate arises from clouds, their interactions with radiation, and their role in the hydrological cycle. Clouds can both absorb and reflect solar radiation (thereby cooling the surface) and absorb and emit long wave radiation (thereby warming the surface) (Houghton et al., 2001). The water vapour budget of the climatically sensitive region of the upper troposphere is greatly influenced by the amount of cloud ice and its vertical distribution (Lynch et al., 2002). Improved observations of the ice water content of clouds and the vertical distribution of these clouds are required to assess and improve the treatment of cloud/radiation interaction and the hydrological cycle in GCMs.

Passive mm/sub-mm has some advantages compared to other space-borne cloud-ice remote sensing techniques. Solar reflectance and thermal infrared methods are inherently sensitive to optical depth, while mm/sub-mm radiometry is more directly sensitive to ice water path and particle size because the wavelengths are similar to the sizes of cirrus ice crystals. Visible and near infrared solar reflection methods can't distinguish ice from underlying liquid water cloud, can't measure low optical depth clouds over brighter land surfaces, and only work during daytime. Solar techniques also retrieve an effective radius which is biased to the cloud top for thick clouds, and are highly sensitive to uncertainties in the nonspherical particle phase function. Thermal infrared methods saturate for moderate optical depths and can only determine effective radius for small crystal sizes. 94 GHz Cloud profiling radar can penetrate very thick cirrus, but as with all single frequency techniques, it is susceptible to uncertainty in the particle size distribution. Another limitation is poor sampling from the lack of horizontal scanning ability. With multiple wavelengths chosen from the mm/sub-mm region it is possible to manage the penetration/sensitivity tradeoff , while giving sensitivity to a broad enough range of the particle size distribution to constrain size distribution parameters and detect most of the cloud ice mass.

We define the cloud induced radiance as the difference between the observed radiance and that for the same atmosphere without clouds, $\Delta I = I_{cloudy} - I_{clear}$. A complicating factor in using mm/sub-mm wavelengths to observe cirrus, is that the particle/radiation interaction is dominated by scattering. For downlooking geometries, this tends to result in ice cloud decreasing the observed radiance, hence negative ΔI. For limb sounding the sign of ΔI can change from negative to positive with increasing tangent height. This sign change reflects the changing role of clouds in limb radiances from scattering radiation away from the line of sight to scat-

Correspondence to: Cory Davis (cdavis@staffmail.ed.ac.uk)

tering radiation into the line of sight. This description, where scattering is the dominant process, is in contrast to the situation with liquid water clouds, and rainfall at low microwave frequencies, where the hydrometeors are mainly absorbing, and passive microwave observations over ocean yield a positive ΔI. Scattering complicates the radiative transfer (RT) part of the retrieval problem. Unlike clear sky remote sensing applications, where scalar RT without scattering can be applied and the solution is a simple path integral, the inclusion of scattering introduces polarisation and an influence from atmospheric properties outside the line of sight, and hence a requirement of 3D geometry for a complete treatment. 3D RT calculations are computationally demanding, and the field of 3D RT is an area of considerable current research effort. Consequently, in remote sensing applications, where the speed of the 'forward model' can be critical, 3D polarised RT has not been used. Instead, the approximations of a 1D spherical shell, or plane-parallel atmosphere are often made, and polarisation is neglected.

In this work we use a state-of-the-art radiative transfer model (ARTS-MC), on a detailed midlatitude cirrus scenario, to give simulated observations for three different space-borne instruments: the Advanced Microwave Sounding Unit - B (AMSU-B), the Cloud Ice Water Sub-millimetre Imaging Radiometer (CIWSIR), and the Earth Observing System Microwave Limb Sounder (EOS-MLS). As well as demonstrating the capability of the radiative transfer software to perform such detailed simulations, the results indicate the extent to which cloud inhomogeneity affects the radiances observed by these instruments, and the extent of polarisation effects caused by particle shape. The cloud-inhomogeneity and polarisation effects will have follow-on effects on cloud ice retrievals dependent on 1D unpolarised forward models.

To identify any influence of cloud inhomogeneity, comparisons were made between 3D RT and 1D representations of the 3D scenario. Any differences arising between 3D and 1D have two main causes: 1. FOV averaging over radiances that are in the large optical path / non-linear RT regime will cause a systematic bias compared to a 1D representation with equivalent FOV averaged cloud optical path. 2. Actual 3D radiative transfer effects resulting from photon transport perpendicular to the viewing direction through inhomogeneity not present in the 1D representations. Effect 1 has been called *beamfilling* by previous authors, particularly with regard to passive microwave retrievals of rainfall rate (e.g. Wilheit et al. (1977), McCollum and Krajewski (1998), Kummerow (1998)) and liquid water path in non-precipitating clouds (e.g. Lafont and Guillimet (2004)). To help attribute any observed 1D/3D difference to either beamfilling or 3D radiative transfer effects, simulations were also performed using the Independent Pixel Approximation (IPA), which treats each incoming direction within the FOV as a unique 1D RT calculation. Since, like the 3D simulations, the IPA simulations also integrate over the FOV with the 3D heterogeneous cloud field, the beamfilling effect will be observable. However the confinement of photons along a single path eliminates 3D radiative transfer effects . Where there is good agreement between 3D and IPA, yet significant differences between 3D and 1D, the beamfilling effect is dominant.

2 The Models

All simulations were performed using the Monte Carlo scattering component of the Atmospheric Radiative Transfer Simulator (ARTS-1-1-*) software package, which we refer to as ARTS-MC. ARTS-MC includes the algorithm described by Davis et al. (2005a), which performs 3D polarised radiative transfer for pencil-beam cases. More recently, a generalisation of this algorithm has been included, which allows for surface reflection and field of view (FOV) averaging. Naturally, the surface contributions and antenna pattern integration are performed using Monte Carlo integration (MCI) with importance sampling.

The purpose of the independent pixel approximation (IPA) RT calculations was to provide FOV averaged IPA calculations for comparison with 3D RT to investigate the magnitude of true 3D RT effects. IPA simulations were performed with a slightly modified version of the generalised Monte Carlo algorithm described above. The main point of difference lies in the looking-up of optical properties. As for the generalised Monte Carlo code, a reversed multiply scattered photon path is traced through the 3D domain. However, the optical properties, which determine pathlength, scattering angle, and emission or scattering events, are obtained from the point on the original reversed propagation path with the same pressure as the point in question.

To avoid difficulties in comparing different models, the 1D simulations were also performed using the 3D Monte Carlo model, expanding a 1D field (varying only with pressure) over the 3D grid.

3 Scenario

3D IWC fields were obtained from example output of Robin Hogan's cloudgen software (http://www.met.rdg.ac.uk/clouds/cloudgen/). This takes cloud radar data, in this case from the Chilbolton radar on 17 July 1999, and applies a stochastic method (Hogan and Kew, 2005) to generate a 3D field from the 2D (height, time) observations. Other required fields e.g. temperature, water vapour, height, were obtained from collocated ECMWF Operational Analysis data. The cloudgen grid was 256 by 256 by 64, corresponding to a resolution of approximately 780 m by 780 m by 110 m. This fine grid was merged with a coarser grid, wide enough to satisfy the condition that all photons not emitted in the atmosphere must enter either from the top of the atmosphere or the surface. Fig. 1 shows the approximate surface footprints for the simulations.

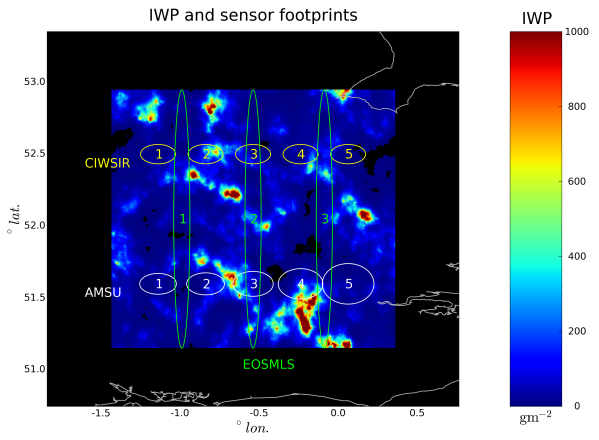

Fig. 1. Ice water path (IWP) for the 17 July 1999 cloudgen scenario. Approximate footprints for each simulation are also shown.

In each case the instrument antenna response function was 2D Gaussian, with the zenith and azimuth full width half maximum (FHWM) corresponding to the instruments concerned. Fig. 2 shows a side view of the viewing beams used in the simulations.

To look at how polarisation responds to different particle aspect ratios or degrees of ice crystal horizontal alignment, we consider horizontally aligned oblate spheroids with aspect ratios 1.3 and 3.0. This range was chosen arbitrarily. The appropriate value for midlatitude cirrus is unknown due to a lack of dual polarised observations at these frequencies. Davis et al. (2005b) showed dual polarised EOSMLS 122 GHz ice cloud observations, which were consistent with simulations having particle aspect ratios of 1.2±0.15. However, the generality of this result is limited due to the frequency used; firstly, because O_2 absorption limited the observations to tropical ice cloud reaching over ~ 9 km, and secondly the wavelength restricts sensitivity to only the larger ice particles. For the purpose of reproducing cloud induced radiance and polarisation signals, varying the aspect ratio of oblate spheroids is a reasonable proxy for the variation of shape and orientation distribution for realistic cirrus particles, since for downlooking geometries, where the polarisation is dominated by dichroism, the important parameters are the K_{jj}, and K_{12} extinction matrix elements. Optical properties were calculated using the PyARTS python package (http://www.met.ed.ac.uk/ cdavis/PyARTS), which incorporates the T-matrix code of Mishchenko (both fixed (Mishchenko, 2000) and random (Mishchenko and Travis, 1998) orientations). The McFarquhar and Heymsfield (1997) size distribution, which depends on IWC and temperature, was assumed, and non-spherical particles were related to the size distribution using volume equivalent radius.

4 Instruments

In this study we simulated observations for 3 satellite borne passive instruments operating in the mm/sub-mm range. Two of these AMSU-B and EOSMLS, are designed to measure clear-sky atmospheric variables, with clouds mainly being an impediment to the focus measurements but with some cloud information produced as a secondary by-product. The other instrument, CIWSIR, is a proposed instrument designed specifically for observing cloud ice.

The Advanced Microwave Sounding Unit -B (AMSU-B) is designed to allow the calculation of the vertical water vapour profiles. The instrument has full width half maximum (FWHM) of 1.1°. The antenna provides a cross-track scan, scanning 48.95° from nadir with a total of 90 Earth fields-of-view per scan line. For these simulations we have chosen 190.31 GHz, which lies at the upper limit of channel 20. This choice was made to enhance the sensitivity of the simulated observation to cirrus. For these simulations 5 viewing angles are chosen ranging from 5 to 45 degrees.

CIWSIR (Cloud Ice Water Sub-millimetre Imaging Radiometer) is an instrument proposed for a recent ESA call for Earth Explorer Missions. This is a conical scanning radiometer with a viewing angle of 53°. 12 Channels are used to obtain sensitivity to a range of particle sizes such that the instrument is sensitive to a large majority of the ice mass within cirrus For these simulations we choose example frequencies, 334.65 GHz, and 664 GHz. We consider the antenna to be 2D Gaussian with FWHM of 0.377°.

The Earth Observing System Microwave Limb Sounder (EOSMLS) is onboard the NASA Aura Satellite, which was launched on 15 July 2004. EOSMLS has radiometers at frequencies near 118, 190, 240, and 640 GHz and 2.5 THz. EOS MLS can observe cloud-induced radiances in all of these radiometers. The EOS-MLS IWC product uses cloud induced radiances from the 240 GHz radiometer. In these simulations we choose 230 GHz, which corresponds to a window channel in the lower side band. For the 240 GHz radiometer, the zenith FWHM is 0.061°, and the azimuth FWHM is 0.121°. The 240 GHz radiometer measures only the H-polarised component of the limb radiance.

5 Simulation details

The radiance error in all simulations is 0.2 K, with the exception of EOSMLS 3 km tangent height, for which the error is 0.5 K. ΔI therefore has an error ($= \sqrt{\delta I^2_{cloudy} + \delta I^2_{clear}}$) of 0.28 and 0.71 respectively. The Monte Carlo simulations use as many photons as is required to reach these accuracies. Consequently viewing directions with larger cloud optical path tend to have longer computing times. For the 3D AMSU-B simulations the simulations took between 8 and 24 minutes on a single 3.2 GHz CPU. The CIWSIR simulations took between 9 and 48 minutes. The EOSMLS simulations

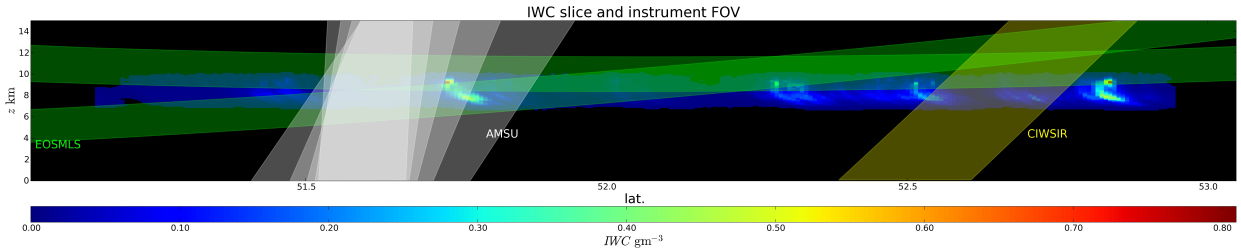

Fig. 2. Side view of an IWC slice and AMSU-B(white), CIWSIR(yellow), and EOSMLS(green) FOV beams.

were generally more expensive for a given accuracy, possibly due to the increased cloud-path. The 3 km EOSMLS simulations (0.5k error) took between 10 and 25 minutes, the 10k simulations took between 108 and 167 minutes.

6 1D representation

If we wish to investigate the effects of cloud inhomogeneity on microwave observations by comparing 3D simulations with 1D, we need to choose an appropriate method for representing the actual 3D cloud structure in one dimension (in our case pressure). If radiative transfer is in the linear regime (low τ_c), the 1D and 3D cases should give similar results if the FOV averaged τ_c is the same for 1D and 3D cases. Therefore, the goal when producing 1D scenarios for comparison with 3D simulations, is to provide 1D scenarios with equal field of view averaged cloud optical path $\bar{\tau_c}$. The calculation of $\bar{\tau_c}$ can be transformed to a volume integration over radius (r), latitude (δ), and longitude (λ) coordinates, and thereby expediting its numerical computation in the ARTS pressure, latitude, longitude grid system.

$$\begin{aligned}\bar{\tau_c} &= \int_{FOV} a\tau_c d\Omega \\ &= \int_{FOV} \int a K_{11} ds d\Omega, \end{aligned} \tag{1}$$

where K_{11} is the (1,1) element of the extinction matrix, which is summed over all particle sizes, shapes, and orientations. If we recognise that this is almost a volume integral, with

$$dV = s^2 ds d\Omega = r^2 \cos(\delta) dr d\delta d\lambda, \tag{2}$$

where s is the distance from the sensor and r is the distance from the earth centre, we get

$$\begin{aligned}\bar{\tau_c} &= \int\int\int \frac{r^2}{s^2} a K_{11} \cos(\delta) dr d\delta d\lambda \\ &= -\frac{R}{g} \int\int\int \frac{r^2}{s^2} a K_{11} \cos(\delta) T d\log p d\delta d\lambda, \end{aligned} \tag{3}$$

where we have used the hydrostatic equation to replace the radius coordinate with $\log p$, and the limits of integration span the cloud scene. K_{11} is represented as the sum of products of particle number densities N_i and K_{11}^i for a finite number of particle sizes. From 3, the following expression for averaging number densities for each particle size over each constant pressure surface will result in $\bar{\tau_c}$ equal to the 3D case.

$$N_i^{1D(p)} = \frac{\int\int \frac{r^2}{s^2} a N_i^{(p)} \cos(\delta) T d\delta d\lambda}{\int\int \frac{r^2}{s^2} a \cos(\delta) T d\delta d\lambda} \tag{4}$$

7 Results

Figures 3 to 7 show the cloud induced radiance, ΔI, and $Q = I_v - I_h$, the second element of the Stokes vector, for all simulations.

Compared to the simulations for the other instruments, the magnitude of ΔI and Q for AMSU-B are small. ΔI for 3D, IPA, and 1D agree within model error. For FP4, Q for 3D and IPA agree well. However, the magnitude of Q is larger for the 1D simulation. The magnitude of ΔI and, to a larger extent, Q, increases for the more aspherical particles.

For all CIWSIR footprints, at both frequencies, the agreement between 3D and IPA results is very good. Also, for footprints where $|\Delta I|$ is small, footprints 3-5, there is little difference between 1D and 3D. For 334.65 GHz this difference is within model error. Where there are noticeable differences between 1D and 3D, the magnitude of ΔI and Q are larger for 1D simulations, and the relative difference tends to be greater for Q. The 1D representation over-estimates ΔI by up to $\sim$ 75% and Q by up to 120% (FP1). The magnitude of ΔI and , to a much larger extent, Q, increases for the more aspherical particles.

For EOSMLS, the 240 GHZ radiometer has an H-polarisation, so the level 1 radiances will not be the total radiance I, but $I - Q$. The MLS observed cloud signal is $\Delta T_H = \Delta I - Q$, which has also been plotted in Figs. 6–7. For the 3 km tangent height simulations, the above comments for CIWSIR apply. The 3D-IPA agreement is good for all footprints, while for FP2 and FP3, which have larger cloud optical path than FP1, the 1D representation results in an over-estimation of ΔI, Q, and ΔT_H. For 10 km tangent height the agreement between 3D, IPA, and 1D simulations is

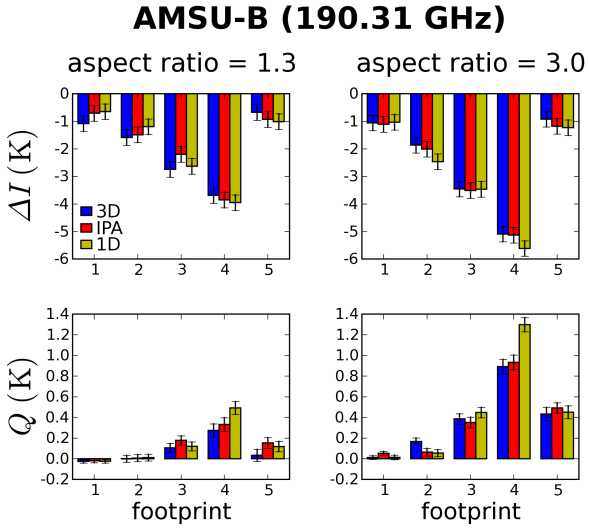

Fig. 3. Simulation results for AMSU-B: ΔI (top row) and $Q = I_v - I_h$ (bottom row), for the five AMSU-B viewing positions indicated in Fig. 1. Results are shown for full 3D RT (blue), the independent pixel approximation (red), and a 1D representation for each viewing position (yellow). The two columns are for two particle aspect ratios. In every case 3D RT and IPA results agree to within model error. For footprint 4, and aspect ratio = 3, the 1D representation over-estimates Q

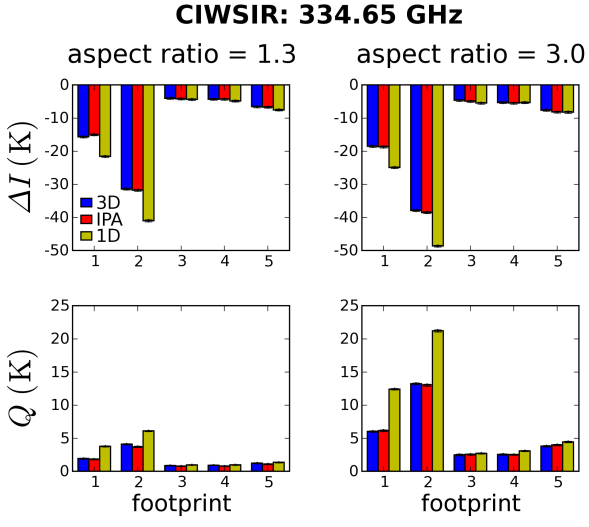

Fig. 4. Simulation results for CIWSIR, 334.65 GHz: Plot layout as for Figure 3. Again there is good agreements between 3D RT and IPA results. For FP1 and FP2 the 1D representation gives increased $|\Delta I|$ and Q. Also note the increase in polarisation signal for the more aspherical particle.

relatively poor. For both tangent heights the magnitude of Q is several times larger for a.r. = 3. For the low tangent heights

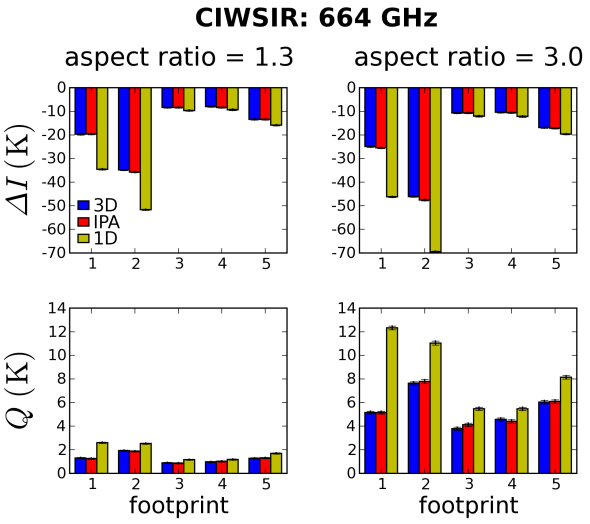

Fig. 5. Simulation results for CIWSIR, 664 GHz: Plot layout as for Figure 3. The same comments for Figure 5 apply here. Note that the increased frequency, and hence cloud optical path has enhanced the 3D and 1D differences.

there is also a small increase in the magnitude of ΔI for a.r.= 3. For the 10 km tangent height, where the signs of ΔI and Q are reversed, increasing the aspect ratio to 3 decreases the brightness temperature enhancement by a factor of 2-3. The resulting H-polarised cloud signal actually observed by MLS is also significantly decreased, by up to a factor of 2 for FP3.

8 Discussion

As demonstrated in Fig. 8 for CIWSIR, the differences between 3D and 1D simulations for the slant viewing instruments, CIWSIR and AMSU-B, and also for low tangent height EOSMLS, increase with increasing FOV averaged cloud optical path $\bar{\tau}_c$.

As $\bar{\tau}_c$ increases two possible mechanisms begin to differentiate 3D and 1D simulations. Firstly, averaging over inhomogeneities in the field of view, where some parts of the field of view have high enough optical path to be in the non-linear radiative transfer regime, will cause 3D scenarios to produce smaller ΔI and Q than 1D representations with equal $\bar{\tau}_c$. This has been called the beamfilling effect in the literature describing passive microwave remote sensing of rainfall rate. Secondly there are 3D radiative transfer effects due to scattering perpendicular to the bore sight path.

The observed behaviour of increasing systematic 1D/3D differences is consistent with the beamfilling effect. The lack of any significant differences between 3D and IPA results indicates that 3D radiative transfer effects are negligible.

In passive microwave retrievals of rain rate, the assumption of homogeneous rainfall across the FOV, coupled with

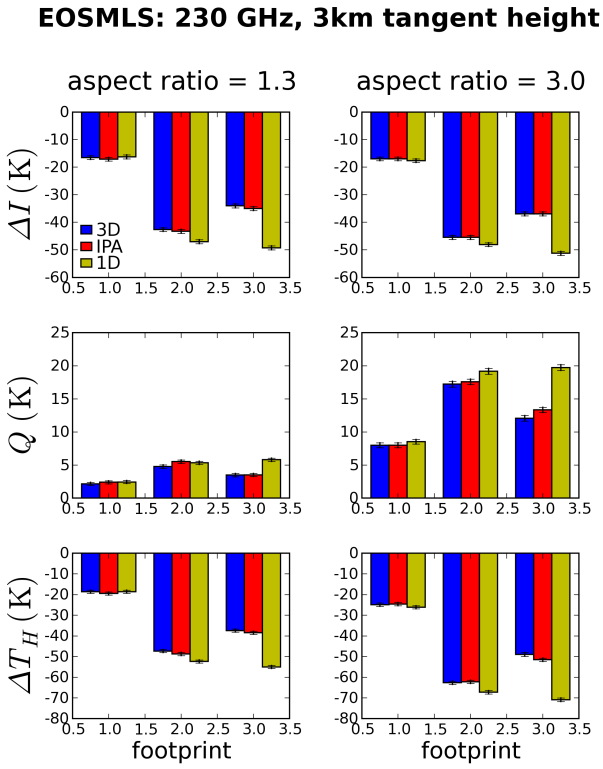

Fig. 6. Simulations results for EOSMLS, 3 km tangent height: Plot layout as for Figure 3. In addition we have plotted the actual H-polarised cloud signal observed by EOS-MLS. Again 3D/IPA agreements is good, and for the two optically thicker cases there are significant 1D/3D differences. Note the significant effect of increased particle aspect ratio on polarisation signal.

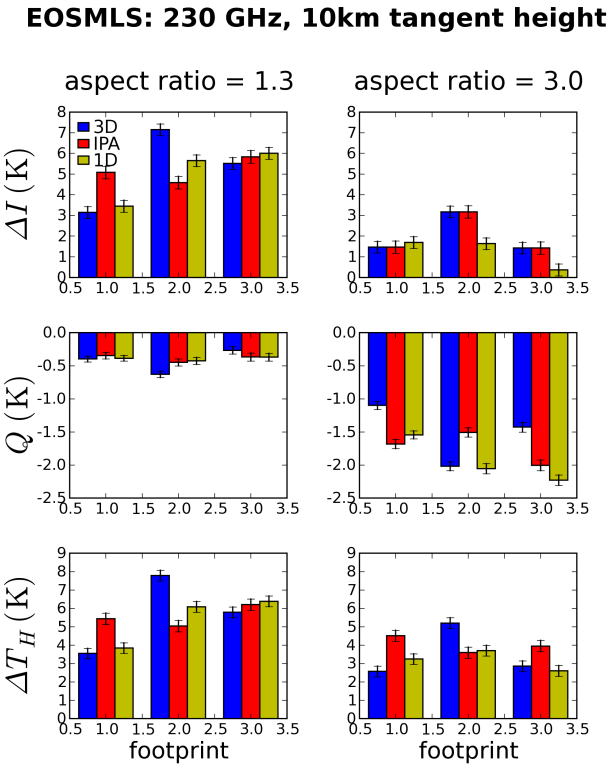

Fig. 7. Simulations results for EOSMLS, 10 km tangent height: Plot layout as for Figure 3. For 10 km tangent height the sign of the cloud induced radiance and polarisation is reversed. Agreement between 3D, IPA and 1D is poor.

the non-linear, concave downwards, response of brightness temperatures to rainfall rate, leads to an underestimates in the retrieved rainfall. This effect has been called beamfilling (Kummerow, 1998; McCollum and Krajewski, 1998; Lafont and Guillimet, 2004). The beamfilling effect was found to be the main source of error in retrieved rainfall rate; a factor of of 2 can exist in the mean rain-rate for a given brightness temperature (Wilheit et al., 1977; Lafont and Guillimet, 2004). The beamfilling effect depends mainly on cloud type, and also on cloud shape, and in all case increases with inhomogeneity and mean LWP or rain-rate (Lafont and Guillimet, 2004). The effect of cloud ice on observed brightness temperature differs from that for rain drops and liquid water cloud because of the complex refractive index and size of the hydrometeors concerned, and also the cloud altitude. Cloud liquid water droplets and raindrops have a high imaginary part of the refractive index, and hence their effect is that of enhanced atmospheric absorption (emission). When viewed over the radiometrically cold ocean, rain and liquid water clouds produce an increased brightness temperature compared with a clear sky. On the other hand cloud ice crystals have only a small imaginary part for the refractive index and particle sizes up to several millimetres, so their effect on brightness temperature is dominated by scattering. In down-looking cases this results in a brightness temperature depression, as radiation from the warmer lower atmosphere is scattered away from the line of sight. Therefore the sign of the cloud signal is reversed from the rainfall/liquid water cloud case. However, like the rainfall and liquid water cloud cases, the magnitude of the cloud signal varies non-linearly (concave-down) with the amount of water in the FOV. This is due to the familiar 'saturation' effect, as the cloud becomes opaque at increased IWP. So with increasing FOV averaged IWP, and increasing inhomogeneity, we might expect beam filling errors in ice cloud observations to become significant. One difference we might expect for ice clouds due to the increased role of scattering is that 3D radiative transfer effects would be more pronounced than for rainfall or liquid water clouds.

We now present a simple mathematical description of the beamfilling effect, which explains the observed differences

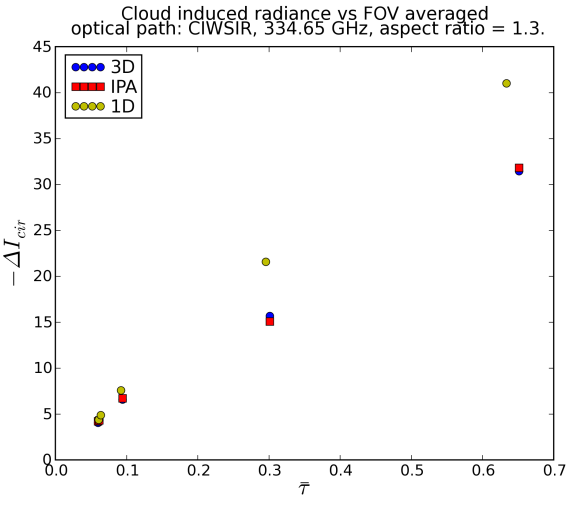

Fig. 8. Cloud induced radiance (ΔI) vs. FOV averaged cloud optical path ($\bar{\tau}$)

between 3D and 1D representations, and also a first-order estimate of the size of the effect that can be compared with our results. We consider the pencil beam cloud induced radiance to be primarily a function of the pencil beam cloud optical path. Here we are considering a downlooking ice cloud observation, where ΔI is negative. For convenience we drop the sign and consider ΔI to be the magnitude of the cloud signal.

$$\Delta I \approx \Delta I(\tau_c) \tag{5}$$

For low optical path, this relationship is almost linear, but due to saturation the curve levels off with increasing optical path, i.e.

$$\frac{d^2\Delta I}{d\tau_c^2} < 0 \tag{6}$$

If we take a Taylor series expansion of the cloud induced radiance about the field of view averaged cloud optical path, $\bar{\tau_c}$ we get the following expression for an actual observation of cloud induced radiance convolved with antenna response function, a.

$$\begin{aligned}
&\int_{FOV} a\Delta I d\Omega \approx \\
&\int_{FOV} a\left[\Delta I\left(\bar{\tau_c}\right) + \left(\frac{d\Delta I}{d\tau_c}\right)_{\bar{\tau_c}}\left(\tau_c - \bar{\tau_c}\right) + \right. \\
&\left.\frac{1}{2}\left(\frac{d^2\Delta I}{d\tau_c^2}\right)_{\bar{\tau_c}}\left(\tau_c - \bar{\tau_c}\right)^2\right] d\Omega \\
&= \Delta I\left(\bar{\tau_c}\right) + \frac{1}{2}\left(\frac{d^2\Delta I}{d\tau_c^2}\right)_{\bar{\tau_c}} \int_{FOV} a\left(\tau_c - \bar{\tau_c}\right)^2 d\Omega \\
&= \Delta I\left(\bar{\tau_c}\right) + \frac{1}{2}\left(\frac{d^2\Delta I}{d\tau_c^2}\right)_{\bar{\tau_c}} \sigma^2_{\tau_c} \\
&< \Delta I\left(\bar{\tau_c}\right)
\end{aligned} \tag{7}$$

This gives a first order description of the beamfilling effect as apparent in the divergent 1D and 3D curves in Fig. 8. We have chosen τ_c as the independent variable here because what we are seeing is a radiative transfer effect, which is most easily understood in terms of τ_c. The same analysis could also be performed using IWP as the independent variable.

The error term above can be calculated for the simulations presented to verify whether the beamfilling effect is the cause of the observed differences. To obtain the second derivative, a pencil beam $\Delta I(\tau_c)$ relationship was obtained using the same scenario but with randomly selected viewing positions and a pencil-beam antenna. The best fit 3rd degree polynomial was found, from which the second derivative in eq. 8 was obtained. This regression is shown in Fig. 9, which also demonstrates, by the horizontal scale, that although $\bar{\tau_c}$ was relatively small (e.g. Fig. 8), individual pencil beams can have high optical paths in the non-linear regime. The variance term is easily obtainable from the standard error of the $\bar{\tau_c}$ calculation.

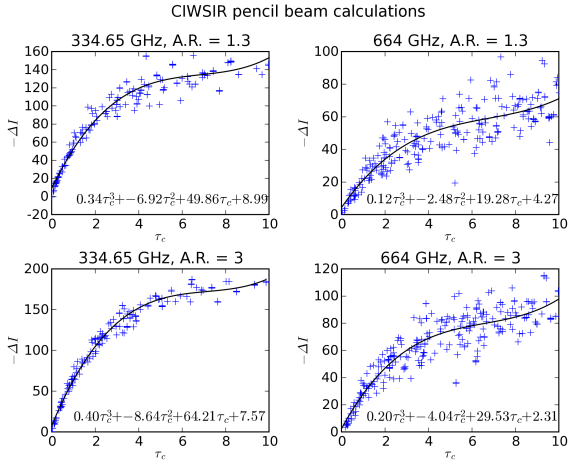

Fig. 9. Finding the best fit relationship between pencil beam cloud induced radiance and pencil beam cloud optical path.

Although the correction term $\frac{1}{2}\left(\frac{d^2\Delta I}{d\tau_c^2}\right)_{\bar{\tau_c}} \sigma^2_{\tau_c}$ seems unsuitable for accurately converting simulated 1D radiances to realistic FOV averaged 3D cases, Fig. 10 indicates that the beamfilling effect is capable of causing the observed 1D/3D differences. Reasons for this lack of accuracy include the approximate nature of the Taylor series expansion and difficulty in obtaining the second derivative of $\Delta I(\tau_c)$, which has considerable scatter for 664 GHz.

These results suggest that CIWSIR and EOSMLS ice cloud observations could be adversely affected by beamfilling. Mitigation of this effect would require a dedicated sim-

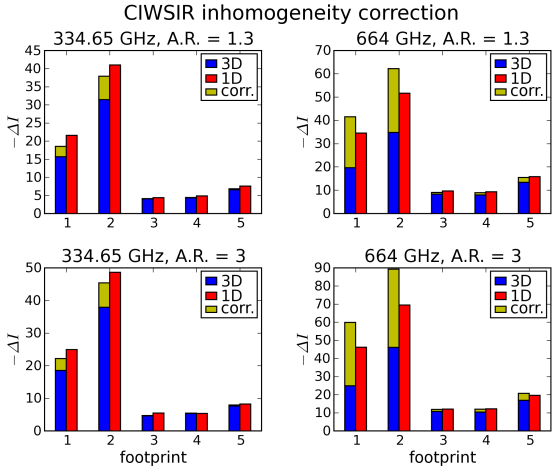

Fig. 10. Comparing the beamfilling correction in eq. 8 against the observed differences.

ulation study. Lafont and Guillimet (2004) found that for microwave rainfall and LWP retrievals, the beam filling effect can be corrected by a simple factor based on sub-pixel cloud cover which could be obtained from collocated visible measurements. With this in mind, a possible beamfilling error mitigation for EOSMLS ice cloud observations would be to utilise other A-train cloud observations, such as those from MODIS and CloudSat, to estimate sub-pixel inhomogeneity and hence the beamfilling error.

As here, Kummerow (1998) demonstrated that for rainfall observations, 3D radiative transfer effects were small, rarely exceeding a few degrees. Given the increased role of scattering in ice observations we might expect 3D RT effects to be bigger. This was not the case in these simulations. A possible explanation for this is that 3D RT effects produce both positive and negative effects on pencil beam radiances, which cancel one another out when integrated over the FOV. As was also noted by Kummerow (1998), the lack of 3D RT effects may not apply where the cloud systems are smaller than the field of view, for example tropical convective clouds.

The 10 km tangent height EOSMLS 3D/1D differences in ΔI and Q are both positive and negative. Also, the IPA and 3D agreement is relatively poor. A major source of the 1D/3D differences for EOSMLS will be due to along-path inhomogeneity, which was also demonstrated by the large 1D/3D differences shown by Davis et al. (2005a). A 1D representation can much better capture along-path inhomogeneity for down-looking or slant geometry than for limb sounding. Also for the high tangent heights, since the cloud signal is caused by scattering into the line of sight, the observation is affected not only by inhomogeneity over the FOV, but also inhomogeneity in the upwelling radiation field. This result suggests that a 3D RT treatment is more important for high tangent height limb sounding than for low tangent heights.

For the slant viewing and low tangent height limb sounding, the positive Q values (and hence partial vertical polarisation) can be described as dichroism. The horizontally polarised component of the upwelling radiation is attenuated by horizontally aligned particles more than the vertically polarised component. For high tangent height limb sounding, the polarisation changes sign to particle horizontal orientation due to H-polarised radiation being preferentially scattered into the field of view. This behaviour was also shown in Davis et al. (2005a). The differences in polarisation behaviour between 1D and 3D simulations is due to the same mechanism as for the 3D/1D ΔI differences: the beamfilling effect. As for ΔI, Q is very similar for the 3D and IPA simulations. For a given aspect ratio, the variation in Q with respect to optical path for down-looking cases is also non-linear concave-down with respect to optical path. Therefore averaging Q over the FOV, where parts of the FOV are in the non-linear radiances regime will also cause systematic differences between 3D and 1D representations.

9 Conclusions

This paper presents the most detailed simulations of spaceborne mm/sub-mm cirrus observations published to date. For this scenario, and the chosen frequencies, AMSU-B simulations were considerably less cloud-sensitive than CIWSIR and EOSMLS due to increased clear sky absorption by water vapour, and also smaller cloud path compared to EOSMLS.

These simulations confirm that the aspect ratio and degree of horizontal orientation of ice crystals will have a significant impact on slant viewing and limb sounding observations. Aspect ratios in the range 1.3 to 3 cause Q in the range 1 to 13 K for CIWSIR:334.65, 1-8 K for CIWSIR:664 GHz, 2-17 K for low tangent height EOSMLS observations, and small ($<$2 K) negative polarisation for high tangent heights. Aspect ratios can also have a noticeable effect on the brightness temperature depression, particularly for high tangent height MLS observations.

For all instruments there are significant differences between 1D and 3D results, but generally good agreement between 3D and IPA. For the the slant looking instruments and for low tangent height limb sounding observations, the 1D/3D difference is systematic, with 1D representations over-estimating the magnitude of both ΔI and Q by an amount that increases with the magnitude of ΔI and hence the cloud optical path. Agreement between 1D and IPA simulations suggests that for slant viewing instruments and low tangent height limb sounding, 3D radiative transfer effects do not have a significant impact on these observations. However, cloud inhomogeneity can have a significant impact through the beamfilling effect. Correcting the beamfilling effect for CIWSIR and EOSMLS cloud observations is a matter for future research.

It should be noted that the results shown are only relevant to midlatitude scenes similar to the one used here. 3D/1D differences for slant and limb viewing could be significantly different or a field of thunderstorms. It is planned to extend this study to tropical scenarios in the future.

Acknowledgements. The authors wish to acknowledge the contribution to this work made by the developers of ARTS and Michael Mishchenko for providing the T-matrix code. Thanks are also due to Robin Hogan for providing the cloudgen software, and for providing the input parameters, which were calculated using observations from the 94-GHz Galileo cloud radar at Chilbolton, which is operated by the Rutherford Appleton Laboratory. The work of Cory Davis is funded by the Natural Environment Research Council.

References

Davis, C., Emde, C., and Harwood, R.: A 3D Polarized Reversed Monte Carlo Radiative Transfer Model for mm and sub-mm Passive Remote Sensing in Cloudy Atmospheres, IEEE Trans. Geosci. Remote Sensing, 43, 1096–1101, 2005a.

Davis, C., Wu, D., Emde, C., Jiang, J., Cofield, R., and Harwood, R.: Cirrus Induced Polarization in 122 GHz Aura Microwave Limb Sounder Radiances, Geophys. Res. Lett, 32, L14 806, 2005b.

Hogan, R. J. and Kew, S. F.: A 3D stochastic cloud model for investigating the radiative properties of inhomogeneous cirrus clouds, Q. J. R. Meteorol. Soc., 131, 2585–2608, 2005.

Houghton, J., Ding, Y., Griggs, D., Noguer, M., van der Linden, P., Dai, X., Maskell, K., and (eds.), C. J.: IPCC, 2001: Climate Change 2001: The Scientific Basis. Contribution of Working Group I to the Third Assessment Report of the Intergovernmental Panel on Climate Change, Cambridge University Press, 2001.

Kummerow, C.: Beamfilling Errors in Passive Microwave Rainfall Retrievals, Journal of Applied Meteorology, 37, 356–370, 1998.

Lafont, D. and Guillimet, B.: Subpixel fractional cloud cover and inhomogenety effects n mocrowave beam filling error, Atmospheric Research, 72, 149–168, 2004.

Lynch, D., Sassen, K., Starr, D. O., and Stephens, G.: Cirrus, Oxford University Press, 2002.

McCollum, J. and Krajewski, W.: Investigations of error sources of the Global Precipitation Climatology Project emission algorithm, J. Geophys. Res., 103, 28 711–28 719, 1998.

McFarquhar, G. and Heymsfield, A.: Parametrization of tropical ice crystal size distributions and implications for radiative transfer: Results from CEPEX, J. Atmos. Sci., 54, 2187–2200, 1997.

Mishchenko, M.: Calculation of the amplitude matrix for a nonspherical particle in a fixed orientation, Applied Optics, 39, 1026–1031, 2000.

Mishchenko, M. and Travis, L.: Capabilities and limitations of a current FORTRAN implementation of the T-matrix method for randomly oriented, rotationally symmetric scatterers, J. Quant. Spectrosc. Radiat. Transfer, 60, 309–324, 1998.

Wilheit, T., Chang, A., Rao, M., Rodgers, E., and Theon, J.: A satellite technique for quantitatively mapping rainfall rates oer the oceans, J. Appl. Meteorol., 16, 551–560, 1977.